From Lipid Dynamics to Precision Predictions: A New Approach Method for Precision Modeling of Phosphoinositide Signaling

Gonzalo Hernandez-Hernandez[1,2], Mindy Tieu[2], Pei-Chi Yang[1,2], Oscar Vivas[5], Timothy J. Lewis[4], L. Fernando Santana[2] and Colleen E. Clancy*[1,2,3]

[1]Center for Precision Medicine and Data Science,
[2]Department of Physiology and Membrane Biology,
[3]Department of Pharmacology,
[4]Department of Mathematics,
University of California, Davis, California
[5]Department of Physiology and Biophysics, University of Washington, Seattle, Washington

*Corresponding author
Email: ceclancy@health.ucdavis.edu

Author Contributions: G.H.H., C.E.C., and PC.Y. designed the research study, conducted simulations, acquired data, analyzed data, and wrote the manuscript. M.T., O.V., L.F.S., and C.E.C analyzed data and wrote the manuscript. O.V. provided experimental data.

Competing Interest Statement: The authors declare no competing interests.

Classification: Biological Sciences, Biophysics and Computational Biology

Keywords: Phosphoinositide Signaling, New Approach Methodologies (NAMs), Precision Medicine

Abstract

Precision medicine requires models that can translate rich molecular measurements into individualized predictions of biological response. Phosphoinositide signaling disorders present an acute challenge, where nonlinear dynamics vary across cell types and are difficult to predict or interpret from measurements alone without mechanistic modeling. We developed a sensitivity analysis-guided New Approach Methodology (NAM) using a multi-step framework and applied it as a proof-of-concept to phosphoinositide signaling. We constructed and optimized a kinetic model of PIP, PIP_2, and IP_3 dynamics using superior cervical ganglion neuron data, then validated it against independent dose-dependent responses without refitting. We then performed local and global sensitivity analyses to identify dominant parameter drivers of pathway behaviors. Sensitivity-guided parameter variation generated a population of model variants that captured lipid dynamics observed in tsA201 cells, human neuroblastoma cells, and hippocampal neurons. To infer cell-specific models, we implemented two complementary inverse approaches: sensitivity fingerprinting guided by mechanistic sensitivities and a neural network trained on synthetic phosphoinositide time series. Both approaches reproduced experimental PIP, PIP_2, and IP_3 dynamics across cell types while preserving the baseline model structure. Importantly, the inferred models correctly predicted experimentally observed responses to kinase perturbation without additional fitting: hippocampal neurons with large basal PIP pools maintained signaling under PI4K inhibition, whereas cells with small pools exhibited failure, validating the framework. Simulations of PI4KA and PIP5K1C loss-of-function mutations under repeated stimulation revealed progressive signaling collapse in small-pool cells but sustained function in large-pool cells, demonstrating that basal lipid composition determines genetic vulnerability. The NAM provides a predictive, cell-specific framework for translating dynamic lipid measurements into mechanistic models that support precision medicine applications in phosphoinositide-related disorders.

Introduction

Precision medicine aims to tailor treatment by accounting for patient-to-patient variation in genes, proteins, and cellular physiology, differences that are averaged out in traditional approaches. Achieving this goal requires not only richer molecular measurements but also dynamic, mechanistic models that can translate measurements into individualized predictions of biological response. Computational New Approach Methodologies (NAMs) provide a path toward this translation by replacing animal experiments with predictive, data-driven modeling frameworks capable of patient and cell-specific inference. This need is acute in lipid signaling disorders, where nonlinear pathway dynamics and chemically diverse lipid intermediates make mechanistic interpretation difficult without explicit dynamic models (Zandl-Lang et al., 2023). Accordingly, lipid signaling represents both a major challenge and a major opportunity for precision medicine.

Lipidomics represents a critical frontier for precision medicine. Phosphatidylinositol 4,5 bisphosphate (PIP_2) is fundamental to this effort because it acts as a central regulator of cellular signaling, membrane dynamics, and metabolism, and these processes can vary substantially across individuals (Balla, 2013; Viaud et al., 2016). Lipid dysregulation contributes to diseases including cancer, neurodegeneration, and metabolic disorders, making lipid pathways valuable both as biomarkers and as therapeutic targets (Burke et al., 2023). However, lipids remain challenging to study in practice because of their structural diversity, transient dynamics, and strong context dependence, requiring sophisticated tools and multidisciplinary strategies.

PIP_2 plays a primary role in plasma membrane signaling. Sequential phosphorylation of phosphatidylinositol (PI) to phosphatidylinositol-4-phosphate (PIP) and then to PIP_2, catalyzed by PI 4-kinase (PI4K) and PIP 5-kinase (PIP5K), respectively, drives PIP_2 synthesis. Intermediates formed during this process regulate cellular processes that include vesicle trafficking, cytoskeletal remodeling, and receptor signaling (De Camilli et al., 1996; Di Paolo et al., 2004). Hydrolysis of PIP_2 by phospholipase C (PLC) forms diacylglycerol (DAG) and inositol trisphosphate (IP_3), two second messengers that propagate downstream responses (Berridge, 1993, 2009; Berridge & Irvine, 1984, 1989). Rapid turnover and nonlinear feedback regulation of intermediates create a dynamic landscape that challenges traditional prediction techniques. Mechanistic modeling of these dynamics offers an opportunity to link kinase dysfunction to disease-relevant alterations in lipid signaling behavior.

Here, we utilized measurements of PIP, PIP_2, and IP_3 with sufficient temporal resolution for kinetic parameter extraction across multiple cell systems: superior cervical ganglion (SCG) neurons (Kruse et al., 2016), tsA201 cells (Dickson et al., 2013), human neuroblastoma cells (Willars et al., 1998), and hippocampal neurons (de la Cruz et al., 2022). Despite differences in cell type, receptor systems, and experimental protocols, the datasets revealed a qualitatively consistent pathway architecture: rapid PIP and PIP_2 depletion, coordinated IP_3 production, and gradual recovery, all following the same sequence of biochemical reactions. However, the magnitude and kinetics of these responses varied substantially across cell types, reflecting quantitative differences in enzyme expression, lipid pool sizes, and cellular geometry. The shared pathway topology suggested that a common biochemical architecture governs phosphoinositide metabolism, with quantitative differences arising from systematic parameter variation rather than distinct pathway organization. The observation motivated a strategy: optimize a kinetic model to one well-characterized reference dataset, then use sensitivity analysis to guide parameter variation across other cell types.

We next developed a NAM that transforms optimized kinetic models into cell-specific inference tools through systematic sensitivity analysis. The framework integrates ordinary differential equations with multi-start Nelder-Mead optimization (Hernandez-Hernandez et al., 2024; Kernik et al., 2019; Moreno et al., 2016) to establish a reference baseline, then employs local and global PRCC sensitivity analysis to map how individual kinetic parameters control distinct signaling features. The sensitivity structure serves as the foundation for three capabilities: first, population modeling that captures biological heterogeneity through constrained parameter variation; second, interpretable manual parameter fingerprinting guided by sensitivity relationships; and third, automated neural network inference that recovers kinetic parameters directly from experimental time series. By combining mechanistic modeling with sensitivity-guided inference and machine learning, the framework enables both interpretable and scalable construction of cell-specific models from phosphoinositide measurements.

We applied the framework to phosphoinositide signaling by optimizing a kinetic model for SCG neurons, then extending it across cell types. The analysis revealed that basal lipid pool composition determines signaling robustness and disease vulnerability. Simulations of loss-of-function mutations in PI4KA and PIP5K1C, lipid kinases implicated in neurodevelopmental and neuromuscular disorders (Burke et al., 2023; Narkis et al., 2007; Salter et al., 2021; Verdura et al., 2021), showed that identical genetic perturbations produce severe signaling impact in cells with small lipid reserves but allow partial compensation in cells with large reserves. The cell type-dependent predictions demonstrate how computational NAMs can translate genetic variants into mechanistic predictions by linking genotype to cellular phenotype. While demonstrated here with established cell lines, the NAM could be extended to enable patient-specific kinetic fingerprinting: measuring phosphoinositide dynamics in patient-derived cells, inferring cell-specific parameters via sensitivity-guided analysis, and predicting vulnerability to genetic or pharmacological perturbations.

Results

We developed a sensitivity-guided New Approach Methodology (NAM) to transform an optimized kinetic signaling model into a mechanistic inference framework, enabling systematic analysis of cell-specific variability. We demonstrate the computational NAM using phosphoinositide signaling to generate cell-specific models relevant to precision medicine applications. We built and optimized a kinetic model using one reference cell type and validated it with independent measurements. Sensitivity analysis mapped parameter-to-phenotype relationships, enabling extension across multiple cell types through population modeling, automated parameter inference with neural networks, and prediction of disease mutation effects in different cellular contexts.

We constructed a kinetic model of PIP, PIP_2, and IP_3 dynamics using differential equations governed by six enzymatic rate constants constrained by biochemical conservation. The model represents lipid phosphorylation, dephosphorylation, PLC-mediated hydrolysis, and IP_3 degradation, while explicitly accounting for IP3 biosensor (LIBRAvIII) binding to map simulated IP3 dynamics to experimentally measurable fluorescence (**Figure 1**). Unless otherwise noted, IP3 traces throughout represent biosensor-bound IP_3 (IP_3-LIBRAvIII), denoted as IP_3*, which is the experimentally measured quantity in most datasets.

The model was optimized using experimental time-course data from superior cervical ganglion (SCG) neurons (**Figure 2A**), where 10 μM Oxo-M applied for 20s activates muscarinic M1 receptors and drives PLC-mediated hydrolysis of PIP_2, producing coordinated depletion of PIP and PIP_2 and generation of IP_3. Six kinetic rate constants (k_{PI4K}, k_{4P}, k_{PIP5K}, k_{5P}, k_{PLC}, and k_{deg}) were estimated using the Nelder-Mead optimization algorithm (**Table 1**). The optimized model reproduced the timing and magnitude of PIP (**Figure 2A-i**), PIP_2 (**Figure 2A-ii**), and IP_3 (**Figure 2A-iii**), transients observed experimentally. The model reproduced experimental dynamics with normalized root mean square errors of 8.9% for PIP, 3.2% for PIP_2, and 4.5% for IP_3, well below the 10% threshold typically considered acceptable for biological time-series fitting.

To validate the model, we tested dose-dependent PIP_2 responses using a different dataset not used in optimization (**Figure 2B**). Agonist concentrations were simulated by adjusting PLC activity levels (PLC_1 = 0.15 for 1.0 μM and PLC_1 = 0.7 for 10 μM Oxo-M) while holding all kinetic parameters constant. The model accurately reproduced experimentally observed PIP_2 depletion measured via IK(M) (KCNQ2/3) tail currents (Kruse et al., 2016) (**Figure 2B-ii**), with approximately 60% depletion at 1.0 μM Oxo-M and 80-90% depletion at 10 μM Oxo-M. The validation supports that six parameters are sufficient to capture the signaling in SCG neurons under different stimulation protocols. The model also captured dose-dependent IP_3 dynamics (**Figure 2B-iii**), explicitly accounting for IP_3 biosensor (LIBRAvIII) binding by distinguishing between free and biosensor-bound IP_3 pools, reproducing both the magnitude and kinetics of IP_3 accumulation and clearance across different agonist concentrations.

We next applied local and global PRCC sensitivity analysis to the optimized superior cervical ganglion (SCG) neuron model to map kinetic parameters to distinct dynamic signaling features. The ±20% parameter variation range was selected to reflect experimental uncertainty in the measured phosphoinositide dynamics from the optimization dataset, providing a biologically relevant window for exploring model behavior. Sensitivity metrics were extracted for three experimentally observable features: minimum PIP, PIP_2 recovery, and peak IP_3* amplitude.

Local sensitivity analysis used a one-factor-at-a-time (OFAT) approach to quantify the isolated effect of each parameter, varying each parameter ±20% independently, while holding all other parameters constant. Minimum PIP was affected by k_{PI4K} and k_{4P} (**Figure 3A-i**), with similar effects from k_{PIP5K} and k_{5P} (**Figure 3B-i**) but minimal effects due to k_{PLC} and k_{deg} (**Figure 3C-i**). PIP_2 recovery exhibited distributed sensitivity across k_{PI4K} and k_{4P} (**Figure 3A-ii**), k_{PIP5K} and k_{5P} (**Figure 3B-ii),** and to a lesser extent k_{PLC} and k_{deg} (**Figure 3C-ii**), indicating that recovery dynamics require coordinated variation across multiple enzymatic steps. IP3* peak amplitude and kinetic variations were masked by trace-wise normalization in panels **3A-C**(iii), but absolute sensitivity is quantified in panel D(iii). IP_3* dynamics were primarily influenced by k_{deg} (**Figure 3C-iii**), which controlled IP_3* decay kinetics. Quantitative OFAT sensitivity metrics for minimum PIP, PIP_2 recovery, and peak IP_3* amplitude are shown in **Figure 3D**, where paired bars reveal asymmetric parameter effects: increasing versus decreasing individual parameters produced different magnitudes of change, reflecting nonlinear pathway dynamics around the baseline operating point.

Global PRCC sensitivity analysis was performed by varying all six kinetic parameters simultaneously by ±20% using Latin Hypercube Sampling to generate 5,000 parameter sets. The model remained stable under combined parameter perturbations and generated a bounded population of signaling responses **(Figure 4A-i, ii, iii)**. Partial Rank Correlation Coefficients (PRCC) quantified how each parameter

influences signaling metrics when all parameters vary together (**Figure 4B**). For minimum PIP **(Figure 4B-i)**, k_{PI4K} and k_{PIP5K} showed positive correlations, while k_{PLC} and k_{4P} showed negative correlations, confirming that PIP levels depend on the balance between synthesis and degradation even under combined parameter variation. For PIP_2 recovery **(Figure 4B-ii)**, k_{PI4K} and k_{PIP5K} showed negative correlations, while all other parameters showed positive correlations, indicating that PIP_2 recovery dynamics require coordinated changes across multiple enzymatic steps. For IP_3* production (**Figure 4B-iii**), k_{PI4K}, k_{PIP5K}, and k_{PLC} showed positive correlations as they drive IP_3 generation through the synthesis pathway, while k_{4P}, k_{5P}, and k_{deg} showed negative correlations by opposing IP_3 accumulation through substrate depletion or degradation. Together, local and global PRCC sensitivity analyses define a clear mapping between kinetic parameters and observable signaling features, with PRCC analysis confirming that parameter effects identified through OFAT persist under combined variation, providing a framework for interpreting cell-to-cell variability.

We next tested whether sensitivity-constrained parameter variation could capture biological heterogeneity across cell types. Rather than refitting the model to each experimental dataset, we generated a population of model variants by varying each kinetic parameter by ±20% relative to the SCG baseline model. The ±20% range was selected to represent within-cell-type biological variability, providing a reference for identifying systematic cross-cell-type differences. Each model variant was evaluated using the stimulation protocol and experimental conditions specific to each cell type.

In SCG neurons, the model population reproduced the observed range of PIP, PIP_2, and IP_3* dynamics under 10 μM Oxo-M stimulation for 20s, establishing a reference distribution for identifying cell-type-specific parameter variations (**Figure 5A**). In tsA201 cells exposed to the same ligand and stimulation duration, experimental trajectories showed deeper PIP and PIP_2 depletion than the SCG-derived model population (**Figure 5B**). These differences aligned with parameters controlling lipid synthesis and turnover, including k_{PI4K}, k_{4P}, k_{PIP5K}, and k_{5P}. In human neuroblastoma cells stimulated with 1 mM carbachol for 60s, experimental responses showed deeper PIP_2 depletion and faster PIP_2 recovery than the SCG population (**Figure 5C**). These dynamics extended beyond the population distribution, indicating parameter variations exceeding the ±20% range. In hippocampal neurons stimulated with 10 μM L-glutamate for 50s, PIP remained stable with no depletion due to larger basal PIP pools, while PIP_2 and IP_3* dynamics were captured by the SCG population (**Figure 5D**). Across all cell types, sensitivity-constrained population modeling revealed structured and feature-specific differences, highlighting specific enzymatic steps that vary across cellular contexts.

We next asked whether sensitivity structure could guide explicit parameter inference from experimental data. Guided by local sensitivity analysis from **Figure 3** and steady-state basal lipid pool compositions, we adjusted parameters for tsA201, neuroblastoma, and hippocampal models to generate cell-type-specific parameter fingerprints (**Figure 6A**). We then trained a hybrid convolutional neural network-long short-term memory (CNN-LSTM) neural network to map phosphoinositide time series to kinetic parameters. Because some experimental trajectories extended beyond the ±20% range, the network was trained using synthetic data generated by varying the SCG baseline parameters by ±40% to ensure robust prediction across the full range of observed biological variability (**Figure 6B**). When applied to experimental measurements, both approaches inferred parameter sets that reproduced observed PIP, PIP_2, and IP_3* dynamics across cell types (**Figure 6C–E**). Inferred parameters were consistent across methods, particularly for k_{PI4K}, k_{4P}, and k_{PIP5K}, which accounted for much of the observed cell-type variability. Together, sensitivity-constrained inference enabled bidirectional mapping between phosphoinositide

263 dynamics and kinetic parameters, supporting direct construction of cell-type-specific signaling models
264 from experimental measurements.
265
266 Having established that cell-type-specific parameter variations could be systematically identified and
267 quantified, we next asked whether this framework could predict signaling perturbations associated with
268 loss-of-function mutations in key phosphoinositide enzymes. We simulated loss-of-function perturbations
269 in PI4KA and PIP5K1C, genes linked to neurodevelopmental disorders with altered phosphoinositide
270 homeostasis, by reducing k_{PI4K} and k_{PIP5K}, respectively, and evaluated signaling responses under repeated
271 receptor stimulation.
272
273 Simulations consisted of three 20-second stimulation pulses delivered at 100s, 600s, and 1100s. In superior
274 cervical ganglion neurons, PI4KA loss-of-function was simulated by reducing k_{PI4K} by 50% and 100%.
275 Under repeated stimulation, PI4K reduction caused progressive depletion of PIP and PIP_2. Recovery failed
276 between stimulation pulses as limited lipid reserves became exhausted. IP_3 responses decreased with each
277 pulse, indicating cumulative pathway failure (**Figure 7A**).
278
279 PIP5K1C loss-of-function was simulated by reducing kPIP5K by 50% and 100%, representing partial
280 enzymatic impairment and complete functional loss, respectively. PIP5K reduction disrupted PIP2
281 synthesis, leading to accumulation of PIP before stimulation and depletion of PIP_2. IP_3 production
282 continued only while existing PIP_2 reserves remained available. Once depleted, IP_3 responses collapsed
283 during subsequent stimulation pulses. In SCG neurons, which maintain small basal PIP pools, both PI4K
284 and PIP5K perturbations produced progressive signaling failure under repeated stimulation (**Figure 7B**).
285
286 We next examined whether the same mutations produced different outcomes in cell types with larger basal
287 PIP pools. Using the same stimulation protocol with 20s pulses at 100s, 600s, and 1100s, simulations were
288 performed in hippocampal neurons, which maintain substantially larger PIP pools than SCG neurons
289 (26,000 vs 4,540 molecules/μm^2, a 5.7-fold difference)(Kruse et al., 2016). In the hippocampal context,
290 k_{PI4K} reduction produced a markedly different response. PIP and PIP_2 recovered between stimulation
291 pulses under both cases of 50% and 100% reduction. IP_3 signaling was preserved across all three pulses,
292 indicating that large basal PIP reserves buffer the effects of reduced PI4K activity (**Figure 8A**).
293
294 PIP5K reduction in hippocampal neurons produced milder phenotypes compared to SCG neurons.
295 Although loss of PIP5K activity ultimately prevented full PIP_2 restoration, larger baseline PIP_2 pools
296 sustained IP_3 responses for longer durations. PIP_2 depletion occurred more gradually, and IP_3 signaling
297 persisted across repeated stimulation before eventual decline. The simulations demonstrate that larger
298 basal PIP pools confer protection against genetic perturbations that cause pathway failure in cells with
299 smaller lipid reserves (**Figure 8B**)
300
301 Together, the simulations demonstrate that the effects of lipid signaling mutations depend on the size of
302 basal phosphoinositide pools. The same genetic perturbation causes severe signaling failure in cells with
303 small lipid reserves but allows partial compensation in cells with larger reserves. By combining sensitivity
304 analysis with kinetic modeling, the sensitivity-guided NAM links mutation effects to cellular biochemical
305 context and enables the prediction of cell-specific vulnerability to signal disruption under genetic
306 perturbation.
307
308

Discussion

Here, we present a computational framework that integrates mechanistic modeling, sensitivity analysis, and parameter inference to predict cell-specific signaling behavior, which together comprise a novel NAM (new approach methodology). Using phosphoinositide signaling as a proof of concept, this work demonstrates how dynamic biochemical measurements can be translated into cell-specific predictive models, provide new disease insights, and serve as a potential tool for precision medicine.

We first validated a kinetic model of PI, PIP, PIP_2, and IP_3 signaling (**Figure 1**). The model includes only the enzymatic steps required to reproduce experimentally measured dynamics and conserves lipid mass across pathway components. Kinetic parameters were optimized and validated using independent experimental datasets from superior cervical ganglion neurons (**Figure 2A, B**). Agreement between model predictions and experimental measurements provided a stable and biologically grounded foundation for subsequent analyses.

Local and global PRCC sensitivity analysis revealed how kinetic parameters subtly control different aspects of signaling, rather than a dominant rate-limiting step (**Figures 3 and 4**). PIP depletion, PIP_2 recovery, and IP_3 production were governed by overlapping but distinct subsets of rate constants (**Figure 3A-E**). Building on this structure, we tested whether sensitivity analysis could guide inference of cell-specific parameters from experimental data. Bounded parameter variation (±20%) generated a population of models that captured phosphoinositide dynamics across multiple cell types without refitting the model (**Figure 5**).

We demonstrated two approaches to determine rate parameters in the model (**Figure 6**). One method used sensitivity analysis to identify the most important parameters that needed to be adjusted to match the data. The other method used a neural network to automatically estimate rates from the data. Both methods were able to closely match the measured changes over time in PIP, PIP_2, and IP_3 in three different cell types (tsA201 cells, neuroblastoma cells, and hippocampal neurons). Because the two approaches gave similar results, this suggests that time-based measurements of lipid signaling contain enough information to uncover real differences in the underlying biology, assuming that model structure is plausible. For the neural network inference method, we trained the model on synthetic datasets that preserved biochemical relationships between lipid pools and enzymatic activity, ensuring biologically realistic parameter estimates even when experimental trajectories extended beyond the ±20 % range.

We next simulated disease-relevant perturbations in PI4KA and PIP5K1C (**Figures 7 and 8**) by implementing variants as a reduction in k_{PI4K} or k_{PIP5K}, to predict how naturally occurring human genetic mutations may alter lipid synthesis by reducing enzyme catalytic activity or lipid abundance, or by impairing membrane recruitment or protein complex stability. PI4KA encodes PI4KIIIα, which generates the major plasma-membrane PI4P pool that supplies PIP_2 synthesis and is regulated through assembly and recruitment of a PI4KIIIα–TTC7–FAM126 complex(Nakatsu et al., 2012; Suresh et al., 2024). Importantly, experimental perturbation of PI4KA shows that it is required to maintain plasma-membrane PIP_2 during strong PLC-coupled receptor stimulation.

A key prediction from the model simulations indicates the role of basal lipid pool composition in determining genetic vulnerability. Under repeated stimulation, cells with small basal PIP pools exhibited progressive depletion of PIP and PIP_2 and collapse of IP_3 signaling when PI4KA or PIP5K1C flux was

reduced (**Figure 7**), whereas hippocampal neurons with larger basal PIP pools retained partial recovery and sustained signaling even under severe perturbation (**Figure 8**). The fragile versus protected behavior is consistent with experimentally observed responses to kinase perturbation. Hippocampal neurons, which maintain large PIP pools (26,000 vs 4,540 molecules per square micrometer in SCG neurons), recover PIP_2 normally even when PI4K is pharmacologically inhibited, whereas cells with small PIP pools cannot recover without active PI4K (de la Cruz et al., 2022). Our simulations reproduce the behavior: reducing k_{PI4K} by 50 to 100% prevents PIP_2 recovery in SCG neurons but has minimal effect on hippocampal neurons (**Figures 7A-ii vs 8A-ii**).

The results provide a mechanistic explanation for tissue-specific disease severity observed in disorders linked to PI4KA and PIP5K1C mutations (Narkis et al., 2007; Salter et al., 2021; Verdura et al., 2021; Burke et al., 2023). While the simulations presented here focus on loss-of-function mutations, PIP5K1C gain-of-function variants have also been reported and are associated with excessive IP_3 production and pathological calcium signaling (Morleo et al., 2023). Extension of the framework to simulate gain-of-function conditions suggests uncontrolled IP_3 generation as a potential mechanism for disrupted signaling and cellular dysfunction.

One future opportunity is to address the limitation that the model presented herein does not explicitly account for the energetic regulation of kinase activity. Because plasma-membrane PIP and PIP_2 can be depleted rapidly under hypoxia and ATP inhibition, the energetic state represents an additional axis of biochemical regulation captured by k_{PI4K} and k_{PIP5K} (Lu et al., 2022). In excitable tissues, ATP can fluctuate on rapid timescales (including beat-resolved ATP dynamics in cardiac myocytes), raising the possibility that ATP microdomains modulate phosphoinositide resynthesis capacity during repeated demand (Rhana et al., 2024). Future extensions incorporating energetic constraints would complement established lipid-homeostatic feedback, such as PIP4K-dependent restraint of PIP_2 synthesis by PIP5Ks (Wang et al., 2019; Wills et al., 2023).

Together, the work demonstrates a New Approach Methodology (NAM) in which mechanistic modeling, sensitivity analysis, and constrained inference translate dynamic lipid measurements into interpretable, cell-specific kinetic parameters for modeling and simulation. In a precision-medicine context, the framework naturally supports a workflow in which a patient genotype is paired with time-resolved PI, PIP, PIP_2, and IP_3 measurements in patient-derived cells to infer effective changes resulting from genetic perturbation. The arrival of increasingly sophisticated biosensors makes this plausible in the not-too-distant future. More broadly, the increasing therapeutic interest in phosphoinositide kinases underscores the value of quantitative, context-aware models for connecting variant mechanisms to predicted signaling phenotypes.

Methods

Phosphoinositide Signaling Model Structure

A system of differential equations was developed to represent the dynamic interconversion of phosphatidylinositol (PI), phosphatidylinositol 4-phosphate (PIP), and phosphatidylinositol 4,5-bisphosphate (PIP_2), as well as the hydrolytic cleavage of PIP2 by phospholipase C (PLC), yielding inositol 1,4,5-trisphosphate (IP_3). The model structure was adapted and simplified from a previously published formulation describing the signaling dynamics in tsA-201 cells and superior cervical ganglion

(SCG) neurons(Falkenburger et al., 2013; Kruse et al., 2016) . The model tracks five dynamic state variables: PIP and PIP_2 on the plasma membrane (molecules/μm²), free cytoplasmic IP_3 (μM), and the genetically encoded IP_3 biosensor LIBRAvIII in both free and IP_3-bound states (μM). PI was treated as a constant pool because PI accounts for more than 90 percent of the total phosphoinositide pool in both superior cervical ganglion neurons and tsA 201 cells (Kruse et al., 2016).

The governing equations for membrane species (molecules/μm²) are:

$$\frac{d[PIP]}{dt} = k_{PI4K} \cdot [PI] - k_{4P} \cdot [PIP] - k_{PIP5K} \cdot [PIP] + k_{5P} \cdot [PIP2] \quad (1)$$

$$\frac{d[PIP2]}{dt} = k_{PIP5K} \cdot [PIP] - k_{5P} \cdot [PIP2] - k_{PLC} \cdot [PIP2] \cdot PLC_1 \quad (2)$$

For cytoplasmic species (μM), the equations describing IP_3 dynamics and biosensor binding are:

$$\frac{d[IP3_{free}]}{dt} = CF \cdot kPLC \cdot [PIP2] \cdot PLC_1 - k_{deg} \cdot [IP3_free] - k_on \cdot [IP3_{free}] \cdot [LIBRAvIII_{free}] + k_off \cdot [IP3 - LIBRAvIII] \quad (3)$$

$$\frac{d[LIBRAvIII_{free}]}{dt} = -k_{on} \cdot [IP3_{free}] \cdot [LIBRAvIII_{free}] + k_{off} \cdot [IP3 - LIBRAvIII] \quad (4)$$

$$\frac{d[IP3-LIBRAvIII]}{dt} = k_{on} \cdot [IP3_{free}] \cdot [LIBRAvIII_{free}] - k_{off} \cdot [IP3 - LIBRAvIII] \quad (5)$$

where the biosensor kinetics parameters k_{on} = 1.0 s^{-1} and k_{off} = 0.5 s^{-1}, were obtained experimentally, yielding an equilibrium dissociation constant K_D = 0.5 μM (Kruse et al., 2016). The conversion factor CF links membrane PIP_2 hydrolysis to cytoplasmic IP_3 production: CF = (S_A / V_{cyt}) × (1/602) = (4100 μm² / 6644 μm³) × (1/602) = 1.03 × 10^{-3} μm^{-1}, where S_A is the plasma membrane surface area, V_{cyt} is the cytoplasmic volume, and 1/602 converts molecules to μM·μm³ (Kruse et al., 2016).

Receptor activation by muscarinic agonist (10 μM oxotremorine-M) was modeled as a step function: PLC_1 = 0.7 (dimensionless activity coefficient) during stimulation and PLC_1 = 0 otherwise. For validation data (Figure 2B), PLC_1 = 0.15 and PLC_1 = 0.7 were used to simulate application of 1.0 μM and 10.0 μM oxotremorine-M, respectively.

Initial conditions at t = 0 were set to experimentally measured basal levels: $[PIP]_0$ = 4540 molecules/μm², $[PIP_2]_0$ = 3232 molecules/μm², $[IP_{3free}]_0$ = 0.02 μM, $[LIBRAvIII_{free}]_0$ = 6.0 μM, and $[IP3\text{-}LIBRAvIII]_0$ = 0.0 μM. The constant PI pool was fixed at [PI] = 226,975 molecules/μm² (Kruse et al., 2016).

The system of five coupled ODEs was solved numerically over $t \in [0, 300]$ s using the MATLAB ordinary differential equation (ode15s) solver with relative tolerance 10^{-6} and absolute tolerance 10^{-10}. Model outputs were compared to experimental measurements of the PIP, PIP_2, and IP_3-LIBRAvIII biosensor signal.

Nelder-Mead Parameter Optimization of the Phosphoinositide Signaling Model

The Nelder-Mead method was used to estimate the kinetic parameters governing the time-dependent behavior of the phosphoinositide intermediates PIP, PIP_2, and IP_3. The system comprises six parameters (k_{PI4K}, k_{4P}, k_{PIP5K}, k_{5P}, k_{PLC}, k_{deg}). Nelder-Mead is a derivative-free optimization method well-suited for biological parameter estimation problems where the cost function landscape contains multiple local minima (Hernandez-Hernandez et al., 2024; Kernik et al., 2019).

The cost function for optimization was defined as the total sum of squared errors (SSE) across all time points:

$$\mathrm{SSE} = \sum_{i=1}^{n}\left[\left(PIP_i^{model} - PIP_i^{data}\right)^2 + \left(PIP_{2_i}^{model} - PIP_{2_i}^{data}\right)^2 + \left(IP_{3_i}^{model} - IP_{3_i}^{data}\right)^2\right] \qquad (6)$$

A bounded transformation confined all parameters to the biologically plausible range of 10^{-8} to 1000. Convergence was declared when both the maximum relative change in all parameters fell below 10^{-4} and the relative change in SSE fell below 10^{-6} between consecutive iterations, with a maximum of 10,000 function evaluations per trial.

To mitigate the risk of convergence to local minima, a multi-start global optimization strategy was employed. Each trial was initialized with a randomly generated parameter vector sampled from log-uniform distributions spanning the allowed parameter range. Upon identifying a local minimum, the parameters were perturbed by independently adjusting each value within ±20%, and the resulting vector was used to initiate a new optimization run. This process was repeated for 1,000 independent trials. The parameter set yielding the lowest total sum of squared errors (SSE) across all iterations was selected as the optimal solution.

Model accuracy was assessed through residual diagnostics. Metrics included the sum of squared errors, the root mean square error, as well as error decomposition by molecular species.

Local Sensitivity Analysis

We performed one-factor-at-a-time (OFAT) local sensitivity analysis to quantify how individual parameter perturbations affect model outputs. For each of the six kinetic parameters (k_{PI4K}, k_{4P}, k_{PIP5K}, k_{5P}, k_{PLC}, k_{deg}), we generated 5,000 model simulations spanning parameter values from 0.8× to 1.2× baseline (corresponding to ±20% variation), matching the experimental uncertainty in SCG neuron baseline measurements. All other parameters were held constant at baseline values during each parameter variation.

Three metrics were calculated from each simulation: (1) minimum PIP, (2) PIP_2 recovery at t=300s (final/initial ratio), and (3) peak IP3 amplitude. Stimulation was 10 μM Oxo-M applied from 80s to 100s.

Global Sensitivity Analysis

To assess parameter interactions and system robustness beyond one-factor-at-a-time (OFAT) analysis, we performed global sensitivity analysis by simultaneously varying all six kinetic parameters (k_{PI4K}, k_{4P}, k_{PIP5K}, k_{5P}, k_{PLC}, k_{deg}), each sampled uniformly in log-space across the ±20% range used for local analysis. We generated 5,000 parameter sets using Latin Hypercube Sampling (LHS), a space-filling quasi-random sampling method that ensures efficient coverage of multidimensional parameter space by dividing each

dimension into N equal-probability intervals, sampling one value per interval, then permuting samples across dimensions to minimize correlation.

To quantify parameter importance in the global analysis, we calculated Partial Rank Correlation Coefficients (PRCCs) between each parameter and output metrics to measure monotonic association strength after removing linear effects of all other parameters. PRCC values range from −1 to +1, where values near ±1 indicate strong monotonic relationships and values near 0 indicate weak or complex non-monotonic effects.

Neural Network Parameter Estimation

To enable rapid parameter estimation from experimental time-series data, we trained a hybrid convolutional neural network-long short-term memory (CNN-LSTM) neural network to predict kinetic parameters from normalized PIP, PIP2, and IP_3 trajectories. Convolutional layers extract local temporal features while LSTM layers capture long-range sequential dependencies across the full-time course. The network comprised two 1D convolutional layers (64 and 128 filters, kernel size 5) with batch normalization and max pooling for temporal feature extraction, followed by a 2-layer LSTM (128 hidden units) to capture sequential dynamics, and three fully connected layers (128, 64, 6 units) for parameter prediction.

Training data consisted of 50,000 simulated trajectories generated using Latin Hypercube Sampling across parameter ranges spanning 0.6× to 1.4× baseline values for all six parameters (k_{PI4K}, k_{4P}, k_{PIP5K}, k_{5P}, k_{PLC}, k_{deg}) and 5 to 50 for the PI/PIP ratio. The expanded ±40% range captured parameter variations observed in cell types beyond SCG neurons, particularly hippocampal neurons and neuroblastoma cells**.** Variable stimulus durations (20, 50, or 60s) matching experimental conditions were encoded as an additional input channel. Each simulation trajectory was interpolated to 100 time points over 300s, with each species (PIP, PIP2, IP_3) normalized independently to its maximum value within that trajectory and paired with its corresponding parameter set as ground truth.

Training used log10-transformed parameters with mean squared error loss, Adam optimizer (learning rate 0.001, weight decay 10^{-5}), batch size 150, and learning rate scheduling using a 90/10 train-validation split. Training proceeded for 100-150 epochs with early stopping (patience = 20 epochs) to prevent overfitting. The model was implemented in PyTorch and trained on GPU when available.

For experimental data prediction, normalized PIP, PIP2, and IP3 time courses were input to the trained network along with stimulus duration. Network outputs in $\log_{10}$ space were converted back to linear scale via $k_i = 10^{y_i}$, where y_i is the network output for parameter i. Predicted parameters were compared to baseline SCG values as percentage changes, then used to generate cell-type-specific models for tsA201, neuroblastoma, and hippocampal neurons.

Simulation protocols

Code for simulations and analysis was written in MATLAB 2018b. The MATLAB optimization routine was run on an Apple Mac Pro machine with two 2.7 GHz 12-Core Intel Xeon processors and an HP ProLiant DL585 G7 server with a 2.7 GHz 28-core AMD Opteron processor. Numerical results were visualized using MATLAB R2018a by The MathWorks, Inc. All codes are available on GitHub (https://github.com/ClancyLabUCD/from-lipid-dynamics-to-precision-predictions)

Declaration of generative AI and AI-assisted technologies in the manuscript preparation process

During the preparation of this work, the authors used ChatGTP and Claude for language editing purposes. After using these tools, the authors reviewed and edited the content as needed and take full responsibility for the content of the published article.

Acknowledgments

This work was supported by National Heart, Lung, and Blood Institute grants 1R01HL174001 (C.E.C, L.F.S.,), R01HL168874 (C.E.C., L.F.S.). National Institute of General Medical Sciences R35GM142690 (O.V.). The UC Davis Chancellor's Postdoctoral Fellowship (G.H.H.) and the UC Davis School of Medicine Center for Precision Medicine and Data Sciences.

References

Berridge, M. J. (1993). Inositol trisphosphate and calcium signalling. *Nature*, *361*(6410), 315–325. https://doi.org/10.1038/361315a0

Berridge, M. J. (2009). Inositol trisphosphate and calcium signalling mechanisms. *Biochimica Et Biophysica Acta*, *1793*(6), 933–940. https://doi.org/10.1016/j.bbamcr.2008.10.005

Berridge, M. J., & Irvine, R. F. (1984). Inositol trisphosphate, a novel second messenger in cellular signal transduction. *Nature*, *312*(5992), 315–321. https://doi.org/10.1038/312315a0

Berridge, M. J., & Irvine, R. F. (1989). Inositol phosphates and cell signalling. *Nature*, *341*(6239), 197–205. https://doi.org/10.1038/341197a0

Burke, J. E., Triscott, J., Emerling, B. M., & Hammond, G. R. V. (2023). Beyond PI3Ks: Targeting phosphoinositide kinases in disease. *Nature Reviews Drug Discovery*, *22*(5), 357–386. https://doi.org/10.1038/s41573-022-00582-5

De Camilli, P., Emr, S. D., McPherson, P. S., & Novick, P. (1996). Phosphoinositides as Regulators in Membrane Traffic. *Science*, *271*(5255), 1533–1539. https://doi.org/10.1126/science.271.5255.1533

de la Cruz, L., Kushmerick, C., Sullivan, J. M., Kruse, M., & Vivas, O. (2022). Hippocampal neurons maintain a large PtdIns(4)P pool that results in faster PtdIns(4,5)P2 synthesis. *The Journal of General Physiology*, *154*(3), e202113001. https://doi.org/10.1085/jgp.202113001

Di Paolo, G., Moskowitz, H. S., Gipson, K., Wenk, M. R., Voronov, S., Obayashi, M., Flavell, R., Fitzsimonds, R. M., Ryan, T. A., & Camilli, P. D. (2004). Impaired PtdIns(4,5)P2 synthesis in nerve terminals produces defects in synaptic vesicle trafficking. *Nature*, *431*(7007), 415–422. https://doi.org/10.1038/nature02896

Dickson, E. J., Falkenburger, B. H., & Hille, B. (2013). Quantitative properties and receptor reserve of the IP(3) and calcium branch of G(q)-coupled receptor signaling. *The Journal of General Physiology*, *141*(5), 521–535. https://doi.org/10.1085/jgp.201210886

Falkenburger, B. H., Dickson, E. J., & Hille, B. (2013). Quantitative properties and receptor reserve of the DAG and PKC branch of G(q)-coupled receptor signaling. *The Journal of General Physiology*, *141*(5), 537–555. https://doi.org/10.1085/jgp.201210887

Hernandez-Hernandez, G., O'Dwyer, S. C., Yang, P.-C., Matsumoto, C., Tieu, M., Fong, Z., Lewis, T. J., Santana, L. F., & Clancy, C. E. (2024). A computational model predicts sex-specific responses to calcium channel blockers in mammalian mesenteric vascular smooth muscle. *eLife*, *12*, RP90604. https://doi.org/10.7554/eLife.90604

Kernik, D. C., Morotti, S., Wu, H., Garg, P., Duff, H. J., Kurokawa, J., Jalife, J., Wu, J. C., Grandi, E., & Clancy, C. E. (2019). A computational model of induced pluripotent stem-cell derived

565 cardiomyocytes incorporating experimental variability from multiple data sources. *The Journal*
566 *of Physiology*, *597*(17), 4533–4564. https://doi.org/10.1113/JP277724
567 Kruse, M., Vivas, O., Traynor-Kaplan, A., & Hille, B. (2016). Dynamics of Phosphoinositide-
568 Dependent Signaling in Sympathetic Neurons. *The Journal of Neuroscience*, *36*(4), 1386–1400.
569 https://doi.org/10.1523/JNEUROSCI.3535-15.2016
570 Lu, J., Dong, W., Hammond, G. R., & Hong, Y. (2022). Hypoxia controls plasma membrane targeting
571 of polarity proteins by dynamic turnover of PI4P and PI(4,5)P2. *eLife*, *11*, e79582.
572 https://doi.org/10.7554/eLife.79582
573 Moreno, J. D., Lewis, T. J., & Clancy, C. E. (2016). Parameterization for In-Silico Modeling of Ion
574 Channel Interactions with Drugs. *PloS One*, *11*(3), e0150761.
575 https://doi.org/10.1371/journal.pone.0150761
576 Nakatsu, F., Baskin, J. M., Chung, J., Tanner, L. B., Shui, G., Lee, S. Y., Pirruccello, M., Hao, M.,
577 Ingolia, N. T., Wenk, M. R., & De Camilli, P. (2012). PtdIns4P synthesis by PI4KIIIα at the
578 plasma membrane and its impact on plasma membrane identity. *Journal of Cell Biology*, *199*(6),
579 1003–1016. https://doi.org/10.1083/jcb.201206095
580 Narkis, G., Ofir, R., Landau, D., Manor, E., Volokita, M., Hershkowitz, R., Elbedour, K., & Birk, O. S.
581 (2007). Lethal Contractural Syndrome Type 3 (LCCS3) Is Caused by a Mutation in *PIP5K1C,*
582 Which Encodes PIPKIγ of the Phophatidylinsitol Pathway. *The American Journal of Human*
583 *Genetics*, *81*(3), 530–539. https://doi.org/10.1086/520771
584 Rhana, P., Matsumoto, C., Fong, Z., Costa, A. D., Del Villar, S. G., Dixon, R. E., & Santana, L. F.
585 (2024). Fueling the heartbeat: Dynamic regulation of intracellular ATP during excitation-
586 contraction coupling in ventricular myocytes. *Proceedings of the National Academy of Sciences*
587 *of the United States of America*, *121*(25), e2318535121.
588 https://doi.org/10.1073/pnas.2318535121
589 Salter, C. G., Cai, Y., Lo, B., Helman, G., Taylor, H., McCartney, A., Leslie, J. S., Accogli, A., Zara, F.,
590 Traverso, M., Fasham, J., Lees, J. A., Ferla, M. P., Chioza, B. A., Wenger, O., Scott, E., Cross,
591 H. E., Crawford, J., Warshawsky, I., … Baple, E. L. (2021). Biallelic PI4KA variants cause
592 neurological, intestinal and immunological disease. *Brain*, *144*(12), 3597–3610.
593 https://doi.org/10.1093/brain/awab313
594 Suresh, S., Shaw, A. L., Pemberton, J. G., Scott, M. K., Harris, N. J., Parson, M. A. H., Jenkins, M. L.,
595 Rohilla, P., Alvarez-Prats, A., Balla, T., Yip, C. K., & Burke, J. E. (2024). Molecular basis for
596 plasma membrane recruitment of PI4KA by EFR3. *Science Advances*, *10*(51), eadp6660.
597 https://doi.org/10.1126/sciadv.adp6660
598 Verdura, E., Rodríguez-Palmero, A., Vélez-Santamaria, V., Planas-Serra, L., de la Calle, I., Raspall-
599 Chaure, M., Roubertie, A., Benkirane, M., Saettini, F., Pavinato, L., Mandrile, G., O'Leary, M.,
600 O'Heir, E., Barredo, E., Chacón, A., Michaud, V., Goizet, C., Ruiz, M., Schlüter, A., … Pujol,
601 A. (2021). Biallelic PI4KA variants cause a novel neurodevelopmental syndrome with
602 hypomyelinating leukodystrophy. *Brain*, *144*(9), 2659–2669.
603 https://doi.org/10.1093/brain/awab124
604 Wang, D. G., Paddock, M. N., Lundquist, M. R., Sun, J. Y., Mashadova, O., Amadiume, S., Bumpus, T.
605 W., Hodakoski, C., Hopkins, B. D., Fine, M., Hill, A., Yang, T. J., Baskin, J. M., Dow, L. E., &
606 Cantley, L. C. (2019). PIP4Ks Suppress Insulin Signaling through a Catalytic-Independent
607 Mechanism. *Cell Reports*, *27*(7), 1991-2001.e5. https://doi.org/10.1016/j.celrep.2019.04.070
608 Willars, G. B., Nahorski, S. R., & Challiss, R. A. J. (1998). Differential Regulation of Muscarinic
609 Acetylcholine Receptor-sensitive Polyphosphoinositide Pools and Consequences for Signaling in

Human Neuroblastoma Cells*. *Journal of Biological Chemistry*, *273*(9), 5037–5046. https://doi.org/10.1074/jbc.273.9.5037

Wills, R. C., Doyle, C. P., Zewe, J. P., Pacheco, J., Hansen, S. D., & Hammond, G. R. V. (2023). A novel homeostatic mechanism tunes PI(4,5)P2-dependent signaling at the plasma membrane. *Journal of Cell Science*, *136*(16), jcs261494. https://doi.org/10.1242/jcs.261494

Zandl-Lang, M., Plecko, B., & Köfeler, H. (2023). Lipidomics—Paving the Road towards Better Insight and Precision Medicine in Rare Metabolic Diseases. *International Journal of Molecular Sciences*, *24*(2), Article 2. https://doi.org/10.3390/ijms24021709

Table 1: Optimized Kinetic Parameters for SCG Neuron Model

Parameter	Nelder-Mead Optimization	Units	Units
k_{PI4K}	0.00078	s^{-1}	PI 4-kinase phosphorylation rate
k_{4P}	0.04019	s^{-1}	4-phosphatase dephosphorylation rate
k_{PIP5K}	0.01626	s^{-1}	PIP 5-kinase phosphorylation rate
k_{5P}	0.02176	s^{-1}	5-phosphatase dephosphorylation rate
k_{deg}	0.06602	s^{-1}	PLC-mediated hydrolysis rate
k_{PLC}	0.24199	s^{-1}	IP_3 degradation rate

Table 1. Optimized kinetic parameters obtained from Nelder-Mead optimization using SCG neuron experimental data (10μM Oxo-M, 20s stimulation). All parameters represent first-order rate constants.

FIGURE LEGENDS

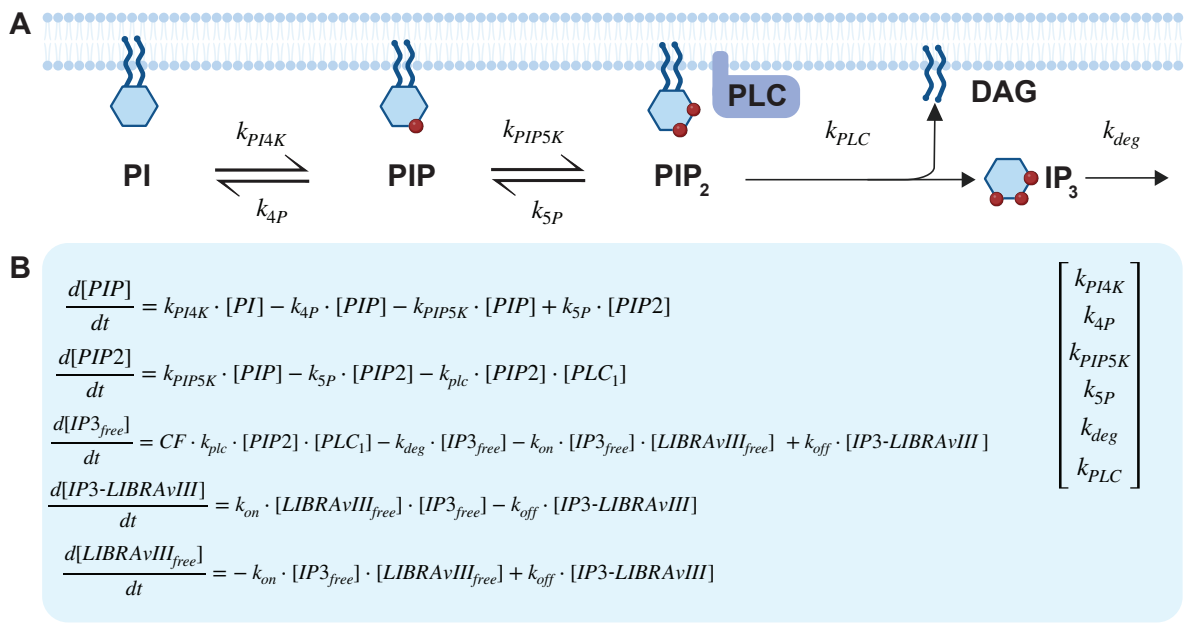

Figure 1. Phosphoinositide signaling pathway and kinetic model. A) Phosphoinositide signaling pathway schematic. Phosphatidylinositol (PI) undergoes sequential phosphorylation to phosphatidylinositol 4-phosphate (PIP) and phosphatidylinositol 4,5-bisphosphate (PIP_2), with dephosphorylation mediated by 4-phosphatase and 5-phosphatase activity. PLC hydrolyzes PIP_2 to generate membrane-bound DAG and soluble inositol 1,4,5-trisphosphate (IP_3). (**B**) Differential equations describing species concentrations (left) with dynamics governed by six kinetic rate constants: k_{PI4K}, k_{4P}, k_{PIP5K}, k_{5P}, k_{deg}, k_{PLC}. The model explicitly includes LIBRAvIII biosensor binding to IP_3, which is accounted for during parameter optimization.

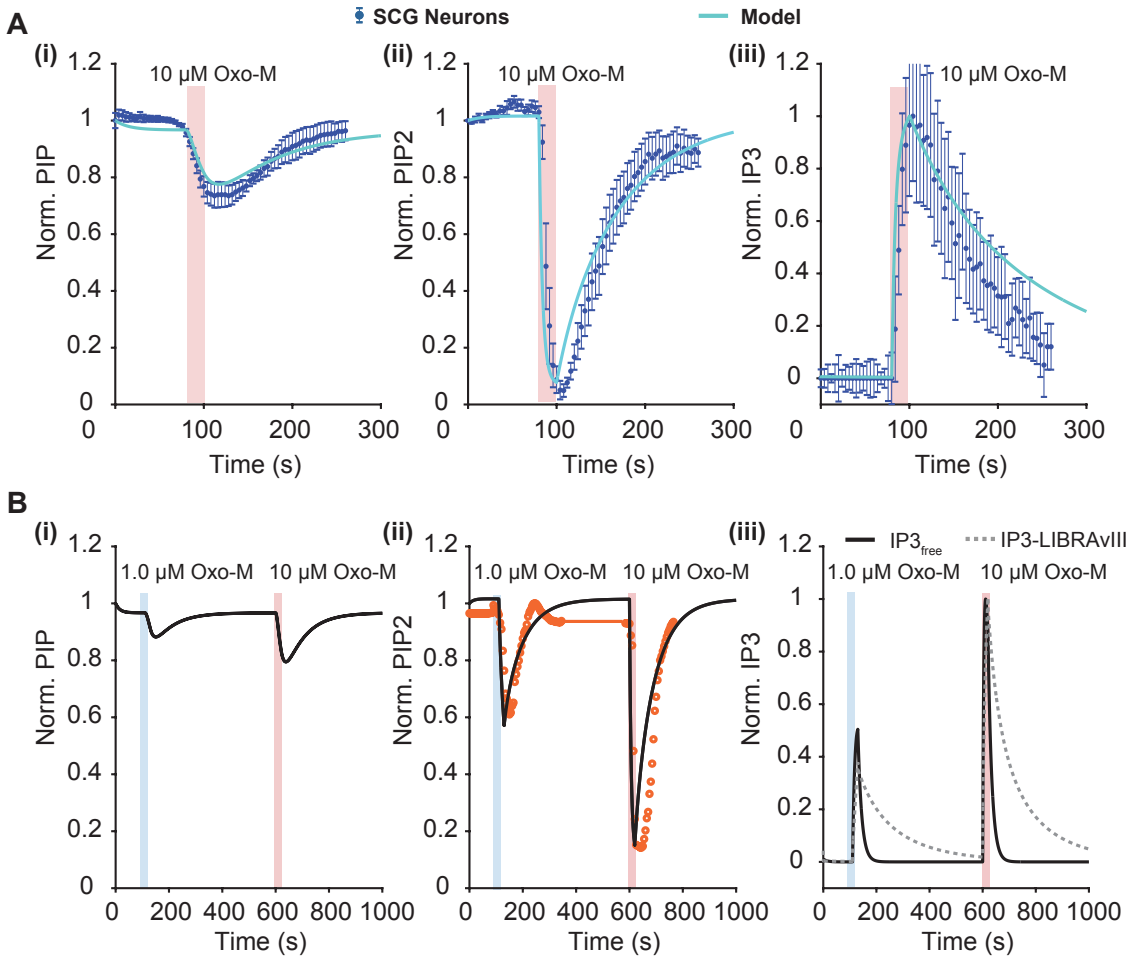

Figure 2. Model optimization and validation in superior cervical ganglion (SCG) neurons. (**A**) Parameter optimization from experimental data (blue symbols; Kruse et al., 2016) following 10 μM Oxo-M for 20 s (pink shading). Six kinetic rate constants (k_{PI4K}, k_{4P}, k_{PIP5K}, k_{5P}, k_{PLC}, k_{deg} were estimated using Nelder-Mead optimization. Model fits are shown as cyan lines for normalized PIP (i), PIP_2 (ii), and IP_3 (iii). (**B**) Model validation using independent PIP_2 data not used in optimization. Using the same kinetic parameters from (**A**) with only PLC concentration adjusted to reflect receptor occupancy, the model predicted dose-dependent PIP_2 depletion at 1.0 μM (blue shading) and 10 μM Oxo-M (pink shading). Experimental PIP_2 measured via IKNCQ2/3 tail current (orange symbols in B-ii, Kruse et al., 2016) matched model predictions: 60% at 1.0 μM and 80-90% at 10 μM, validating the optimized parameters. Model predictions for PIP (i), PIP_2 (ii), and IP_3 (iii) are shown as black lines, with panel (iii) showing free IP_3 (solid) and biosensor LIBRAvIII-bound IP_3 (dashed).

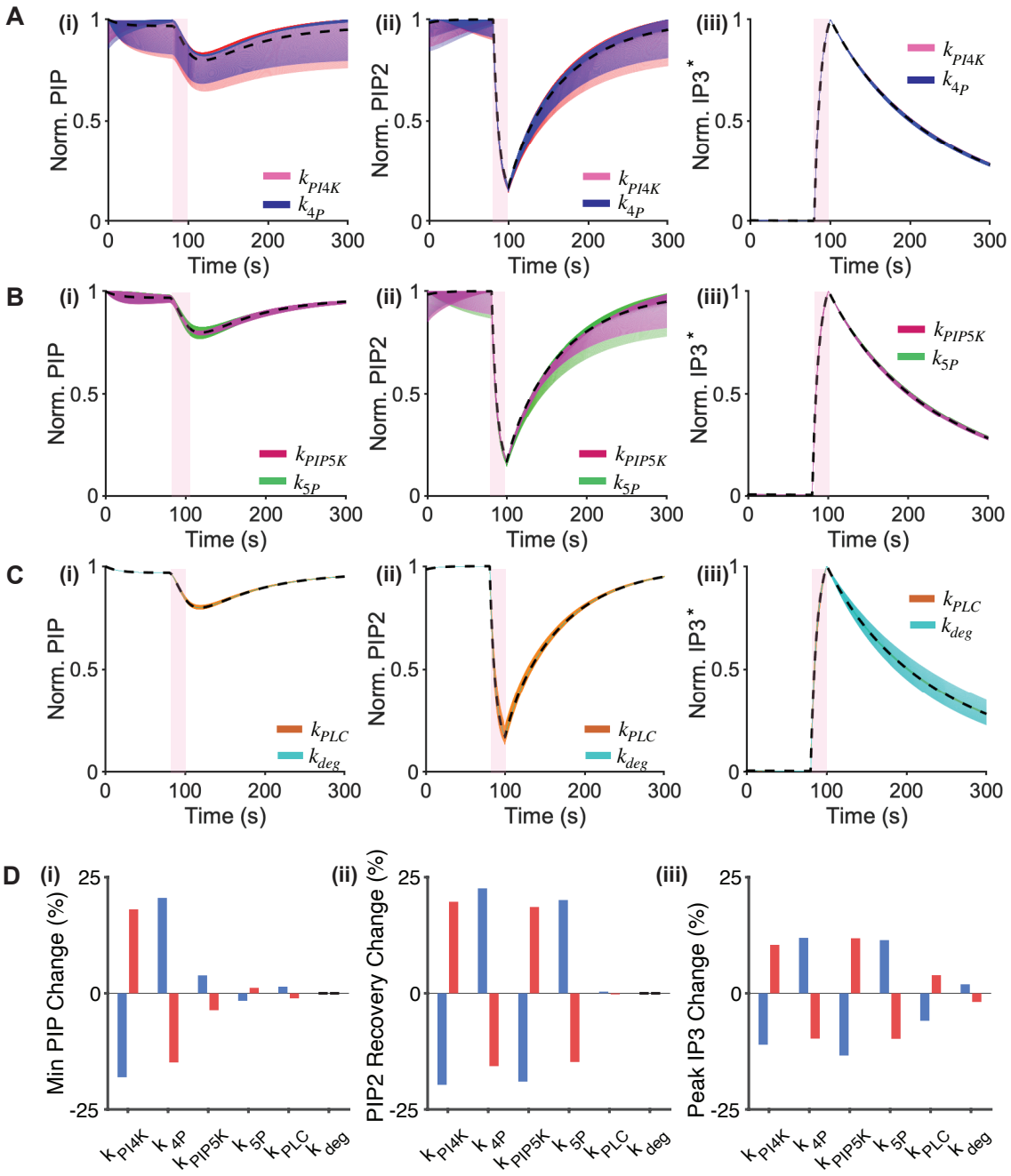
A
(i)
(ii)
(iii)
Norm. PIP
Norm. PIP2
Norm. IP3*
Time (s)
k_{PI4K}
k_{4P}
B
k_{PIP5K}
k_{5P}
C
k_{PLC}
k_{deg}
D
Min PIP Change (%)
PIP2 Recovery Change (%)
Peak IP3 Change (%)
k PI4K
k 4P
k PIP5K
k 5P
k PLC
k deg

Figure 3. Local sensitivity analysis using the one-factor-at-a-time (OFAT) approach. (**A–C**) Local sensitivity analysis of the SCG baseline model from Figure 2A. Each parameter was varied independently by ±20% while holding all others constant, following 10 μM Oxo-M stimulation for 20s (pink shading). Parameters grouped by pathway step: k_{PI4K} and k_{4P} (**A**), k_{PIP5K} and k_{5P} (**B**), k_{PLC} and k_{deg} (**C**). Shaded regions show the range of responses for normalized PIP (i), PIP_2 (ii), and IP_3*(iii). IP_3* represents biosensor-bound IP_3 (IP_3-LIBRAvIII), the experimentally measured quantity. Dashed black lines show the baseline. (**D**) Quantitative sensitivity metrics from OFAT analysis. For each parameter, two bars show the percent change in the metric when that parameter is decreased by 20% (blue bars) or increased by 20% (red bars) relative to baseline. Bar height indicates sensitivity magnitude. Positive bars indicate the parameter change increases the metric; negative bars indicate the parameter change decreases the metric. Metrics shown: minimum PIP (**i**), PIP_2 recovery at t=300s (final/initial ratio) (**ii**), and peak of IP_3 (**iii**).

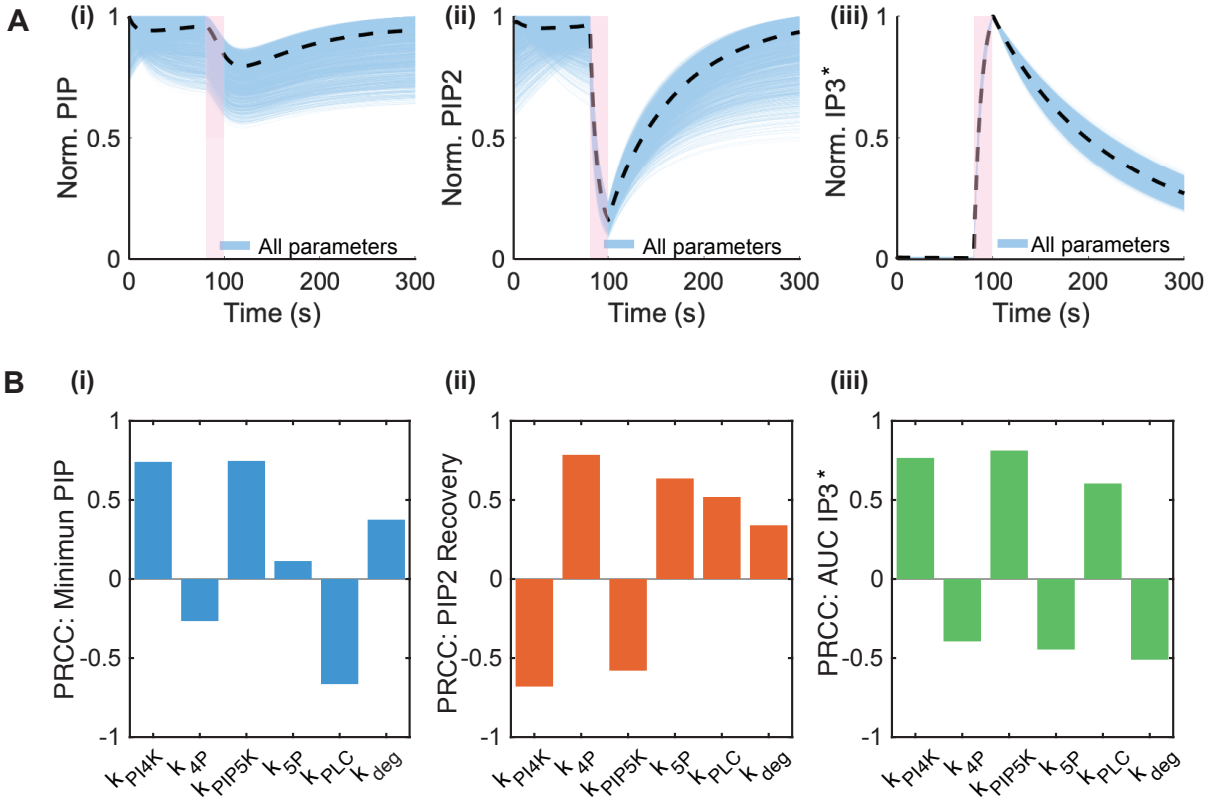

Figure 4. Global sensitivity analysis with all parameters varied simultaneously. (**A**) Model population generated by varying all six kinetic parameters simultaneously by ±20% using Latin Hypercube Sampling (N=5000 parameter sets). Shaded regions show the population envelope for normalized PIP (i), PIP_2 (ii), and IP_3*(iii) following 10 μM Oxo-M stimulation for 20s (pink shading). IP_3* represents biosensor-bound IP3 (IP3-LIBRAvIII), the experimentally measured quantity. Dashed black lines show the baseline model. (**B**) Partial Rank Correlation Coefficients (PRCC) quantifying the strength and the influence of each parameter on signaling metrics when all parameters vary together. PRCC values range from -1 to +1, where magnitude indicates sensitivity strength and sign indicates direction of influence. Metrics shown: minimum PIP (i), PIP_2 recovery (ii), and area under the curve (AUC) IP_3 (iii).

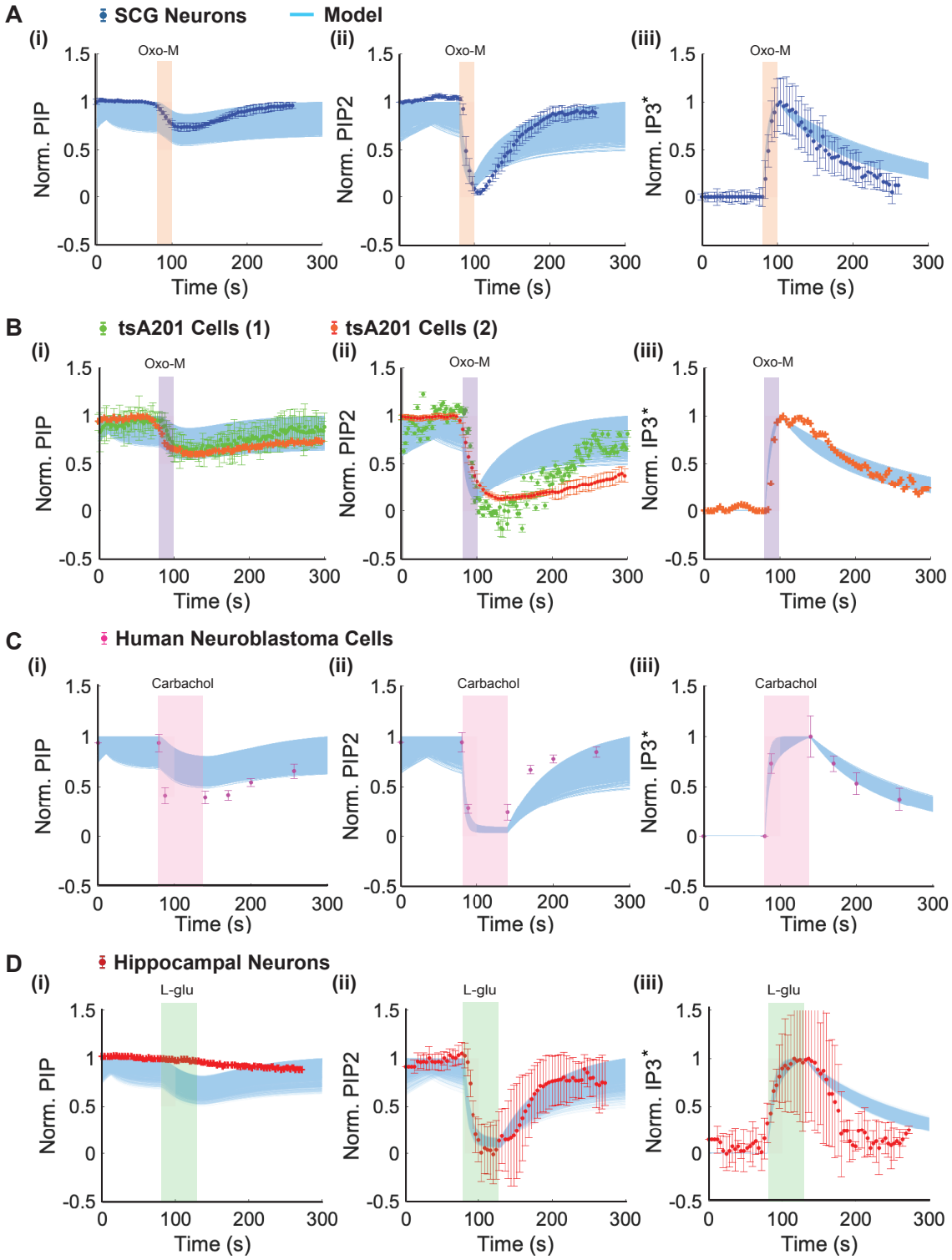
A
SCG Neurons
Model
(i)
(ii)
(iii)
Oxo-M
Norm. PIP
Norm. PIP2
Norm. IP3*
Time (s)
B
tsA201 Cells (1)
tsA201 Cells (2)
C
Human Neuroblastoma Cells
Carbachol
D
Hippocampal Neurons
L-glu

Figure 5. A population of models generated by varying model parameters captures phosphoinositide lipid dynamics in multiple cell types. A population of model variants was generated by perturbing kinetic parameters by ±20% in the SCG baseline neuron model shown in Figure 2A. (**A**) PIP (i), PIP_2 (ii), and IP_3*(iii) dynamics in SCG neurons following 10 μM Oxo-M stimulation for 20s (orange bar). Experimental data (symbols) shown with the model population (shaded region). (**B**) PIP (i), PIP_2 (ii), IP_3* (iii) dynamics in tsA201 cells following 10 μM Oxo-M stimulation for 20s (purple bar). Experimental data from two independent studies (symbols) compared to the SCG-derived model population (shaded region). (**C**) PIP (i), PIP_2 (ii), and IP_3(iii) dynamics in human neuroblastoma cells following 1 mM carbachol stimulation for 60s (pink bar). Experimental data (symbols) compared to the SCG-derived model population (shaded region) using the corresponding stimulation protocol. (**D**) PIP (i), PIP_2 (ii), and IP_3* (iii) dynamics in hippocampal neurons following 10 μM L-glutamate stimulation for 50s (green bar). Experimental data (symbols) compared to the SCG-derived model population (shaded region) using the corresponding stimulation protocol. IP_3* represents biosensor-bound IP_3 (IP_3-LIBRAvIII), the experimentally measured quantity (panels **A**(iii), **B**(iii), **D**(iii)). Panel **C**(iii) shows IP_3 measured by a different method.

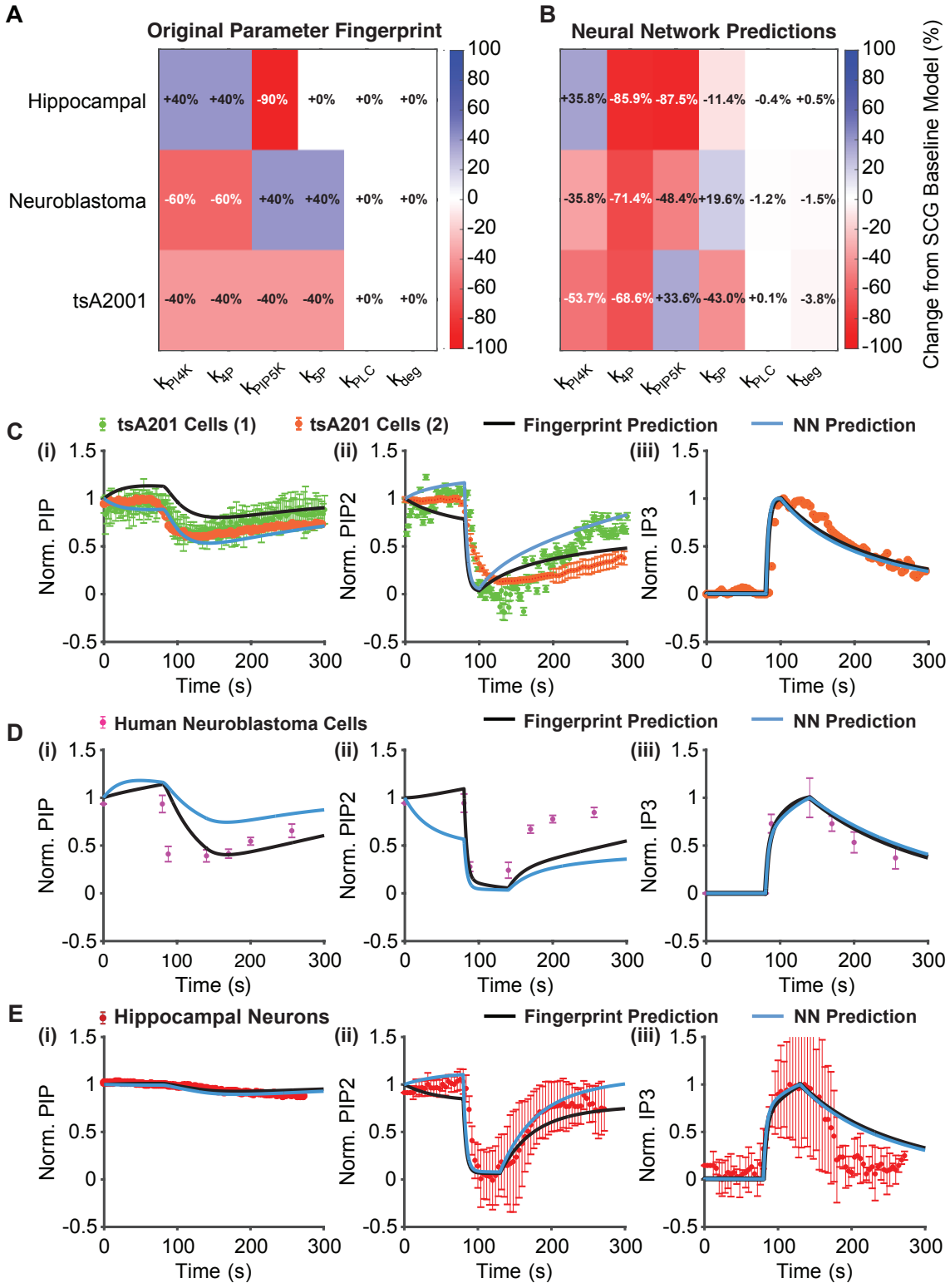
A
Original Parameter Fingerprint
Hippocampal
Neuroblastoma
tsA2001
+40% +40% -90% +0% +0% +0%
-60% -60% +40% +40% +0% +0%
-40% -40% -40% -40% +0% +0%
B
Neural Network Predictions
+35.8% -85.9% -87.5% -11.4% -0.4% +0.5%
-35.8% -71.4% -48.4% +19.6% -1.2% -1.5%
-53.7% -68.6% +33.6% -43.0% +0.1% -3.8%
Change from SCG Baseline Model (%)
C
tsA201 Cells (1)
tsA201 Cells (2)
Fingerprint Prediction
NN Prediction
Norm. PIP
Norm. PIP2
Norm. IP3
Time (s)
D
Human Neuroblastoma Cells
E
Hippocampal Neurons

Figure 6. Parameter inference via sensitivity fingerprinting and neural network inverse modeling. (**A**) Sensitivity-informed parameter fingerprints for each cell type relative to the SCG baseline model from Figure 2A, based on sensitivity relationships (Figure 3) and observed deviations from SCG dynamics. (**B**) Neural network parameter predictions for each cell type relative to the SCG baseline model. The network was trained on synthetic phosphoinositide time series generated by varying SCG baseline parameters ±40%. (**C-E**) Model predictions using fingerprint-derived (black lines) versus neural network-inferred (blue lines) parameters compared to experimental data (symbols). (**C**) tsA201 cells, two independent datasets. (**D**) Neuroblastoma cells. (**E**) Hippocampal neurons. IP_3* (panels **C**(iii) and **E**(iii)) represents biosensor-bound IP_3 (IP_3-LIBRAvIII).

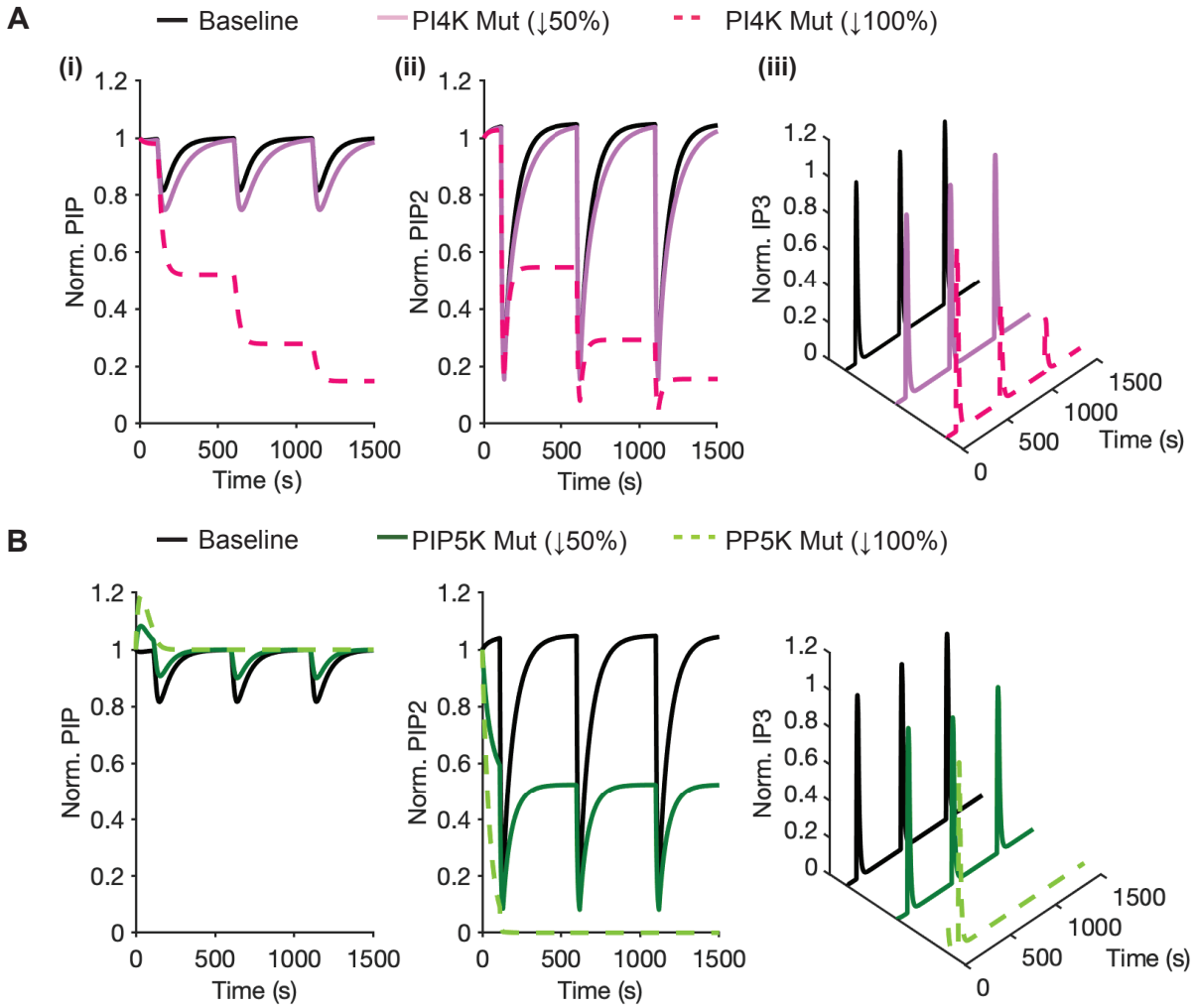

FIGURE 7. PI4K and PIP5K mutations disrupt lipid signaling in SCG neurons. Three 20s stimulation pulses (at 100s, 600s, and 1100s) were applied to the SCG baseline model from Figure 2A. Model predictions shown for PIP (i), PIP_2 (ii), and IP_3 (iii) dynamics. Black lines show the baseline. (**A**) PI4KA loss-of-function simulated by reducing k_{PI4K}. Purple solid line: 50% reduction; pink dashed line: 100% reduction. Progressive PIP and PIP_2 depletion with 100% reduction, showing failed recovery between pulses. (**B**) PIP5K1C loss-of-function simulated by reducing k_{PIP5K}. Green solid line: 50% reduction; green dashed line: 100% reduction. Progressive reduction of PIP_2 synthesis, preventing PIP_2 recovery at 100% inhibition.

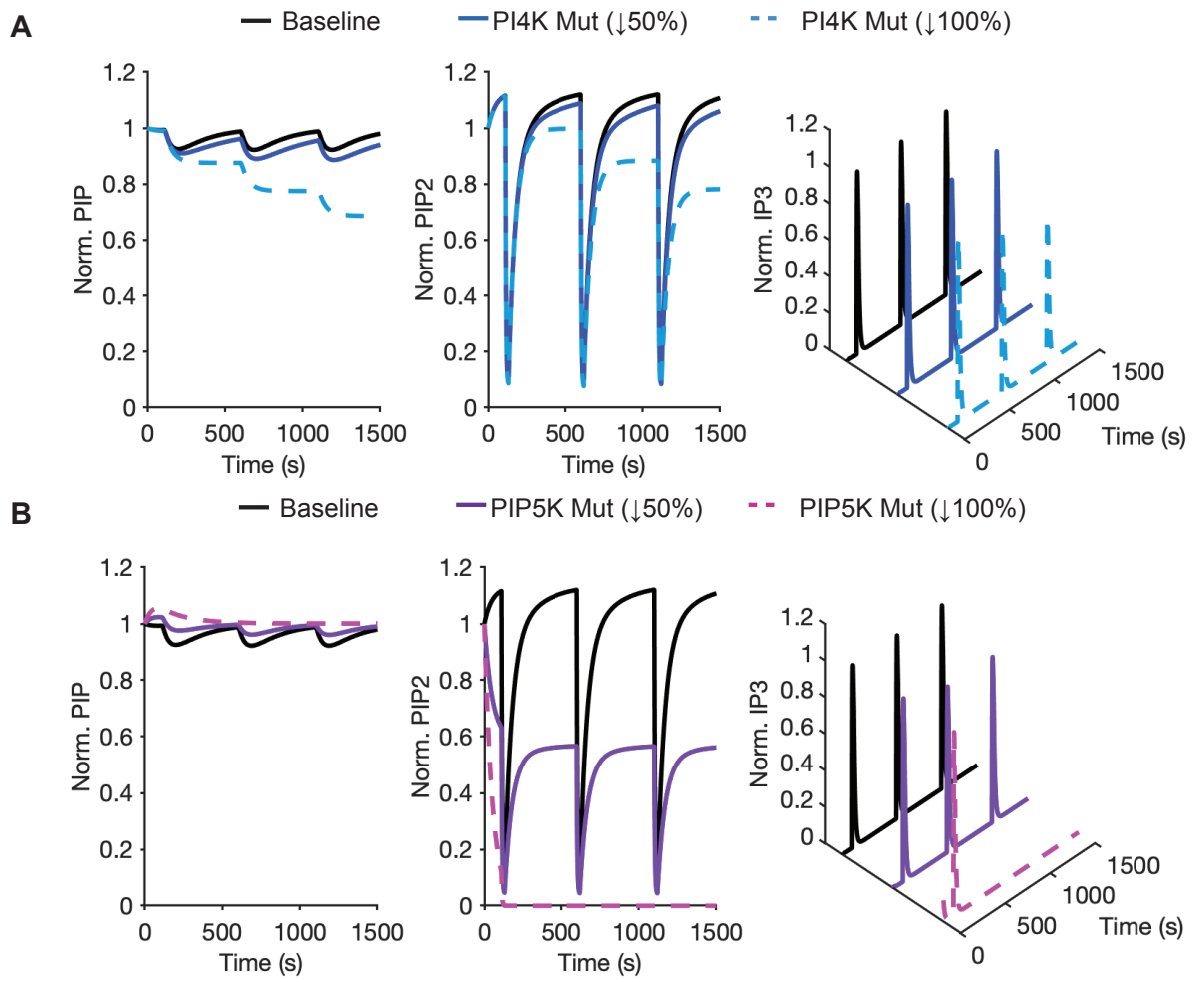

Figure 8. Hippocampal neurons with larger PIP lipid pools are resistant to PI4K mutations. Three 20s stimulation pulses (at 100s, 600s, and 1100s) were applied to the hippocampal neuron model. Hippocampal neurons have much larger basal PIP pools (15.4%) compared to SCG neurons (1.9% in Figure 7). Model predictions for PIP (i), PIP_2 (ii), and IP_3 (iii). Black: baseline. (**A**) PI4KA loss-of-function simulated by reducing k_{PI4K}. Blue solid: 50% reduction; light blue dashed: 100% reduction. PIP and PIP_2 recover between pulses despite 100% mutation. IP_3 signaling was maintained across all three pulses. Larger PIP pools protect against the same mutation that caused failure in SCG neurons (Figure 7A). (**B**) PIP5K1C loss-of-function simulated by reducing k_{PIP5K}. Purple solid: 50% reduction; magenta dashed: 100% reduction. PIP_2 depletion is similar to that of SCG neurons. IP_3 responses sustained longer due to larger baseline pools. Larger lipid pools provide partial protection, though 100% enzyme loss eventually prevents PIP_2 recovery.